Almeida, Humberto; St-Pierre, Luc; Wang, Zhihua; Ribeiro, Marcelo L.; Tita, Volnei; Amico, Sandro C.; Castro, Saullo G.P.

Design, modeling, optimization, manufacturing and testing of variable-angle filament-wound cylinders

Design, modeling, optimization, manufacturing and testing of variable-angle filament-wound cylinders

José Humberto S. Almeida Jr. [a,b,*], Luc St-Pierre [a], Zhihua Wang [c,d], Marcelo L. Ribeiro [e], Volnei Tita [e], Sandro C. Amico [f], Saullo G.P. Castro [c,*]

[a] *Department of Mechanical Engineering, Aalto University, Espoo, Finland*
[b] *Advanced Composites Research Group, School of Mechanical and Aerospace Engineering, Queen's University Belfast, Belfast, UK*
[c] *Faculty of Aerospace Engineering, Delft University of Technology, Delft, The Netherlands*
[d] *School of Mechanical and Electrical Engineering, University of Electronic Science and Technology of China, Chengdu, China*
[e] *Department of Aeronautical Engineering, São Carlos School of Engineering, University of São Paulo, São Carlos, SP, Brazil*
[f] *PPPGE3M/PROMEC, Federal University of Rio Grande do Sul, Porto Alegre, RS, Brazil*

ARTICLE INFO

ABSTRACT

This work demonstrates the potential of manufacturing variable-angle composite cylinders via filament winding (FW), called VAFW. The proposed design strategy allows different filament angles along the axial direction by dividing the cylinder into regions of constant angle called frames. Designs using two, four, or eight frames are herein investigated. A genetic algorithm is applied to optimize each design for maximum axial buckling load. A design with minimum manufacturable filament angle is included in the study. All structures are manufactured and tested under axial compression, with displacements and strains measured by digital image correlation (DIC). The thickness and mid-surface imperfections of the different designs are measured through DIC and used to explain the observed buckling mechanisms. These imperfections are incorporated into a nonlinear numerical model along with a progressive damage analysis. Additionally, a scaling factor is applied on the measured imperfections to enable an imperfection sensitivity study on the proposed designs. The VAFW design shows buckling strength, stiffness, and absorbed energy substantially higher than the constant-angle configuration, attributed to tailored thickness buildup and optimized tow steered angles at particular regions of the cylinder. The experimental and numerical results indicate that VAFW designs can be tailored to postpone buckling so that the material strength can be better exploited.

1. Introduction

Filament winding (FW) is one of the most suitable manufacturing processes for fiber-reinforced solids of revolution [1], such as composite overwrapped pressure vessels [2,3], tubes [4], pipelines [5,6], drive shafts [7], among others. The FW process is well-suited for automation, being fast, cost-effective and compatible with high fiber volume requirements of lightweight and high-performance structures [8]. There are numerous reports in the literature dealing with constant-angle (i.e. constant-stiffness) filament-wound structures, that is, when each layer has a nominal filament angle and a regular thickness distribution [9]. However, recently, Wang et al. [10] designed and optimized for the first time variable-angle filament-wound (VAFW) composite cylinders considering the uncertainties and characteristics of the FW process, and later focused on minimum-mass optimizations constrained by target design loads [11]. Based on that, the present investigation

focuses on the innovative manufacturing and testing of VAFW cylinders, and the possibility of validating numerical models to investigate observed failure mechanisms.

It is already well established that variable-angle configurations (also known as variable-axial [12], variable angle tow – VAT [13], tow-steered [14] and variable-stiffness – VS [15]), in which stiffness can be tailored to follow load paths, are more effective than conventional laminates (e.g., quasi-isotropic laminates) in terms of weight savings, given the higher design freedom due to locally tailored fiber angles [16,17]. Since the establishment of VAT composites by Gürdal and Olmedo [15], this concept is under continuous development by the aerospace sector. For instance, Hao et al. [18] generated the fiber path through linear variation, cubic polynomial, contour lines of cubic function and flow field functions and optimized VS panels for maximum buckling load. The flow field method requires only a few variables to

achieve complicated fiber paths, leading to designs that can be directly manufactured when curvature constraints are used in the optimization. Hao et al. [19–21] also developed integrated optimization frameworks based on isogeometric analysis for VS panels, providing an efficient numerical framework based on the isoparametric concept, which is similar to the finite element (FE) analysis and meshless method. They utilized non-uniform rational B-spline (NURBS) basis functions to discretize the geometric model. In brief, they developed efficient and reliable optimization frameworks at reasonable computational cost, whilst robust enough to generate complex fiber paths, which is hardly possible to reach in a single optimization step using gradient-based methods.

VAT cylinders were first studied by Tatting [22], who analyzed computationally VAT shells in bending with both axial and circumferential angle variations and found significant improvement in terms of critical buckling load. Nevertheless, the first attempt to manufacture a VAT cylinder was performed by Blom et al. [23], exploiting the potential of the automated fiber placement (AFP) process. They also carried out modal tests on non-optimized VAT shells and constant-angle ones with quasi-isotropic (QI) stacking sequence [24]. Blom et al. [25] optimized these shells for buckling load under pure bending by steering fibers along the circumferential direction. These shells were further optimized by the same group [26] with fibers along the axial direction, where the best results were found for cylinders with circumferential stiffness variation, having a bending-buckling capacity 18.5% higher than a QI cylinder of the same weight. At the same time, Wu et al. [27] designed and manufactured VAT shells using graphite/epoxy slit tape material via AFP. Some shells were manufactured with tow overlaps using a cut-and-restart procedure, which penalized the manufacturing efficiency. They reported kinks, waves, and bumps in the tows, but these defects could be avoided by slowing down the fiber placement and increasing the compaction force. Later on, Wu et al. [28] tested $[\pm 45/\pm\theta]_{2S}$ VAT shells under axial compression, where θ is the steering angle that varies along the cylinder circumference. The VAT cylinder with overlaps yielded pre-buckling stiffness and buckling load 62% and 126% higher than the one without overlaps, respectively. They also concluded that VAT shells were less sensitive to geometric imperfections than QI ones. These cylinders were also assessed by White et al. [29], regarding their post-buckling performance. Although the numerical predictions by Wu et al. [27–29] were in good agreement with experimental observations, buckling tests and analyses showed poor correlation, most likely attributed to the presence of geometric imperfections that acted as failure initiator. Later, Wu et al. [30] performed a numerical investigation taking into account geometric imperfections of both shells in their numerical models and concluded that circumferential variations in axial stiffness are responsible for suppressing sensitivity to geometric imperfections, possibly aiding in the agreement between tests and simulation results in their previous works. Rouhi et al. [31] designed and manufactured carbon/epoxy $[\pm\theta/0/90]_S$ VAT cylinders (diameter: 381 mm and length: 762 mm) through AFP, optimized for maximum buckling load in bending using a metamodel-based optimization approach. The baseline for comparison was a QI shell where $\pm45°$ replaced θ. The bending-buckling load was 18.5% higher for the optimized shell compared to the QI one.

The literature review on manufacturing of VA composite cylinders revealed:

- there are no reports on VA cylinders produced via FW, whose main benefits over AFP are related to its higher productivity;
- no studies on the optimization of VAT shells considering fiber angle variations along the axial direction;
- no reports on the variable thickness pattern of VAFW cylinders;
- no investigations dealing with experimental axial compression of filament-wound cylinders, including digital image correlation measurements for a clearer assessment of the buckling mechanism;

- neither measurement nor incorporation of experimentally-measured geometric imperfections into nonlinear FE models of filament-wound structures.

In this context, the present work covers, for the first time, design, modeling, optimization, manufacturing, and testing of VAFW composite cylinders. First, the cylinders are optimized using a genetic algorithm for maximizing their axial compression buckling load by axially varying the angle; Second, the cylinders are manufactured via FW; Prior to the tests, the geometric topography is measured [32] using digital image correlation (DIC); The shells are tested in axial compression assisted by DIC; Finally, experimentally measured geometric imperfection data is used to build numerical models incorporating the observed thickness variation of the as-manufactured specimens [33], along with a progressive damage model that enables a full post-failure analysis used to predict the mechanical response and failure mechanism of the VAFW cylinders.

2. Design and optimization

2.1. Design

Throughout this article, the novel cylinders herein studied are called VAFW. Four designs are investigated:

MA: non-optimized constant-angle cylinder with a winding angle of $\pm50°$, which is the minimum angle (MA) for the utilized mandrel to avoid fiber slippage - Fig. 1(a);

CA: constant-angle with two frames, design variable θ_1^{CA} - Fig. 1(b);

VAFW4: variable-angle with four frames, design variables $\theta_1^{VA4}, \theta_2^{VA4}$ - Fig. 1(c);

VAFW8: variable-angle with eight frames, design variables $\theta_1^{VA8}, \theta_2^{VA8}, \theta_3^{VA8}, \theta_4^{VA8}$ - Fig. 1(d);

2.2. Linear finite element modeling

In this Section, the linear finite element modeling (FEM) is presented in detail. The composite cylinders under investigation here are 300 mm long with a diameter of 136 mm, whose layup consists of an angle-ply layer, $\pm\theta$, nominal thickness of 0.8 mm, i.e. a radius-to-thickness ratio of 85. The experimentally-measured material properties used in all simulations are listed in Table 1, which are representative of towpregs with Toray T700-12K-50C carbon fibers and UF3369 epoxy resin.

The FE models are generated using Abaqus CAE FE package and the models are parameterized via Python scripts. The cylinders are meshed using four-node reduced integration general purpose shell elements (S4R), with three integration points through-thickness for each layer. Previous simulations with full integration were carried out and as the results were the same, elements with reduced integration were chosen given their lower computational costs, crucial for an optimization procedure in which several simulations need to be run. In addition, low-order elements with full integration are more susceptible to either volumetric (typical of incompressible materials with Poisson's ratio higher than 0.5), membrane or shear locking (usually when a structure is under bending), in which the mesh has to be very fine to overcome these locking effects, making both simulation and optimization computationally inefficient.

In order to apply the loads and boundary conditions (BCs), a reference point is set at the center of each free edge of the cylindrical shells and connected using multi-point constraint (MPC), see Fig. 2. This type of constraint was selected to equally distribute the displacement on all nodes connected to the free edges. All degrees-of-freedom are restricted for nodes at the bottom edge ($z = 0$), the top nodes ($z = L$) are only allowed to move axially, and all other degrees-of-freedom are restricted. A buckling load (F_Z) is applied at the top reference point (RP_1). The converged mesh, depicted in Fig. 2, has 152 elements along
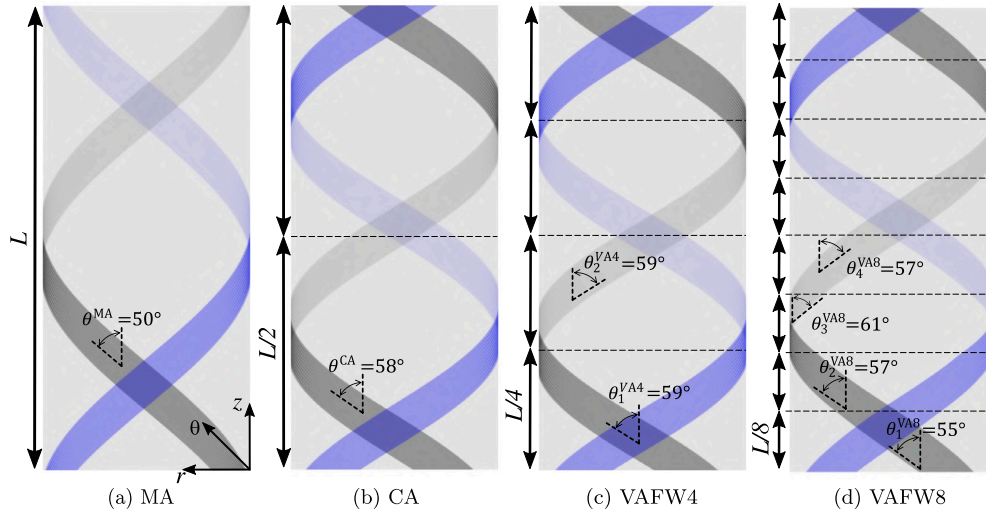
Fig. 1. The filament-wound designs along with the optimum fiber path for each case: side view of the cylinders highlighting the non-optimized design variable(s) for each case, control points (dotted lines) along the shell length (L), and winding trajectories. The shift direction is along the Z (axial) axis.

Table 1
Elastic, strength, and damage properties used in the simulations [34,35].

Property	Description	Value	Property	Description	Value
Elastic	Longitudinal elastic modulus (E_1)	90.0 GPa	Damage evolution	Longitudinal tensile fracture energy (G_T^F)	18 N/mm
	Transverse elastic modulus (E_2)	8.5 GPa		Longitudinal compressive fracture energy (G_C^F)	
	Poisson's ratio in planes 1–2/2–3 ($v_{12} = v_{23}$)	0.32		Transverse tensile fracture energy (G_T^M)	
	Shear moduli in-planes 1–2 and 1–3 ($G_{12} = G_{13}$)	4.3 GPa		Transverse compressive fracture energy (G_C^M)	2 N/mm
	Shear modulus in-plane 2–3 (G_{23})	2.1 GPa			
Strength	Longitudinal tensile strength (X_T)	1409.0 MPa	Damage stabilization	Viscous coefficient in longitudinal tension (η_T^F)	10^{-5}
	Transverse tensile strength (Y_T)	80.0 MPa		Viscous coefficient in longitudinal compression (η_C^F)	
	Longitudinal compressive strength (X_C)	640.0 MPa		Viscous coefficient in transverse tension (η_T^M)	
	Transverse compressive strength (Y_C)	140.0 MPa		Viscous coefficient in transverse compression (η_C^M)	
	Shear strength in plane 1–2 (S_L)	69.0 MPa			
	Shear strength in plane 2–3 (S_T)	44.8 MPa			
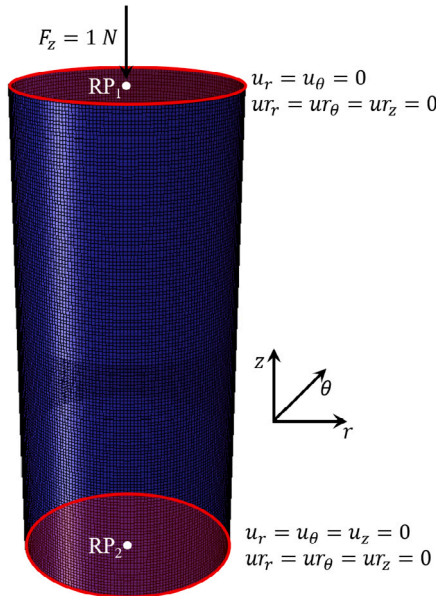
Fig. 2. The applied FE mesh, loads, and boundary conditions.

the axial direction and 213 around the circumference, yielding a mesh with 32,376 elements and 32,589 nodes.

A linear buckling analysis is carried out using Lanczos Eigensolver. The general buckling problem is based on the neutral equilibrium criterion of the total energy potential Π, as follows:

$$\delta^2 \Pi = 0 \tag{1}$$

After derived as per [36,37], a general form is obtained as

$$(\boldsymbol{K} + \lambda \boldsymbol{K}_g) = 0 \tag{2}$$

where $\boldsymbol{K}$ is the constitutive stiffness matrix which depends on the geometry and fiber path; and $\boldsymbol{K}_g$ the geometric stiffness matrix, mostly dependent on the initial stress.

2.3. Optimization

The nature of the optimization considered in this study is a constrained problem, in which the design variables are discrete. For such problems, genetic algorithm (GA) has been proven suitable at finding the global optimum [38] being more effective than gradient-based algorithms that often fall into local minima [39].

Here, the design variables (Section 2.1) are coded as genes using integer numbers, and they are grouped into chromosomes (in form of strings). Given its probabilistic characteristic, populations of possible optimal designs are generated instead of one search point, which is carried out through reproductions, which evolve over generations. An important aspect is that when there are enough search points within the design space, the algorithm is unlikely to fall into local minima. The chromosomes are weighted following the fitness function, which represents the phenotype of that chromosome. The GA algorithm begins with a random population (initial guess); the reproduction is carried out by assessing the fitness function, selecting the best individuals to procreate and generate a larger offspring; in the operations, the genes can be exchanged, which is here carried out using crossovers.
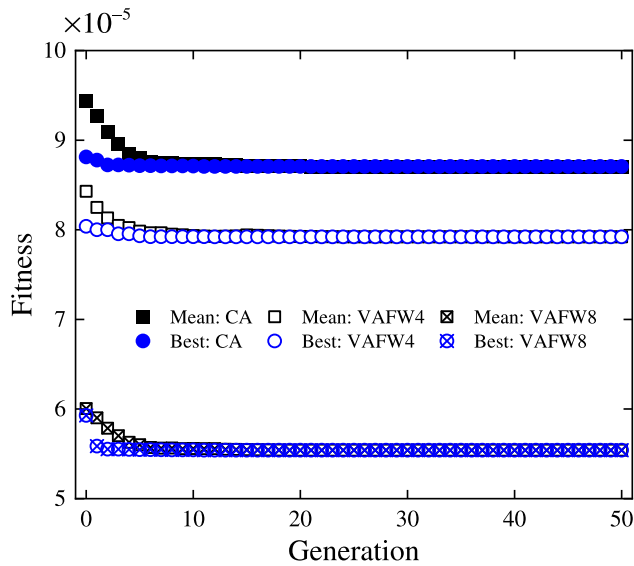
Fig. 3. Convergence plot of the genetic algorithm highlighting the mean and best individuals of each population over the generations for the three optimization cases.

Table 2
Optimal design variables and eigenvalues for each cylinder.

Design	Optimum angles (in degrees)	P_{cr} [N]
MA	⟨50⟩	36,748
CA	⟨58⟩	40,198
VAFW4	⟨59|59|59|59⟩	39,874
VAFW8	⟨55|57|61|57|57|61|57|55⟩	40,363

Table 3
Manufacturing characteristics and final mass of the cylinders.

Design	Degree of covering [%]	Cycles	Band-width [mm]	Pattern number	Mass [g]
MA	101	79			148
CA	101	73	4	8/1	146
VAFW4	101	71			149
VAFW8	104	81			165

with variable stiffness. A similar result was reported in a recent study with VAFW cylinders using an enhanced Kriging metamodel for the optimization [10]. The second VAFW optimized design VAFW8, given in Fig. 1(d), reached the best combination of variable angles to increase the axial buckling capacity.

In the optimization procedure, the fiber angles have one decimal place, but the optimal angles reported in Table 2 are rounded to match with the level of accuracy of the manufacturing process, which in the present study is ±1°, as detailed in Section 3.1. For CA and VAFW4, the optimized angles are respectively 58.4° and 58.6°. Therefore, there is 1° difference between the CA and VAFW4 optimal designs. Nevertheless, it was decided to keep both designs for comparative purposes.

3. Experimental details

3.1. Manufacturing

The cylinders are manufactured by FW with a length of $L = 300$ mm and inner radius $r = 68$ mm. The material used is a towpreg from TCR Composites (USA) composed of Toray T700-12K-50C carbon fibers and UF3369 epoxy resin. The steel mandrel is 400 mm long and the process is performed using a KUKA robot (model KR 140 L100 with MFTech control and peripheral devices) with seven degrees of freedom, that is, with six axes plus the mandrel rotation. The design of the cylinders was performed in CADWIND FW software (from MATERIAL company). The assembly (mandrel plus laminate) is later placed in an oven with air circulation at 105 °C for 24 h. The system is then cooled down to room temperature, and the composite cylinder is extracted from the mandrel. The manufacturing characteristics of each cylinder is presented in Table 3.

To manufacture variable-angle winding paths, the shell is partitioned in frames, as explained in Section 2.1. The winding angles for each design are measured after the first winding cycle to check the suitability of the variable-angle approach, and no angle deviations were observed for the studied design. The precision is ensured by the FW machine, which assists in placing the tows in adjacent frames without the occurrence of slippage. Fig. 4 illustrates the winding process of the VAFW8 cylinder. In traditional FW, each layer requires several cycles to achieve the desired degree of coverage. In every cycle, the tows are deposited with the specified angle for each partitioned frame in the "cylindrical session" of the mandrel and they reach right-angles at the turnaround zone areas to allow deposition of the tow at an angle with opposite sign, forming an angle-ply layer.

A genuine FW process is used in the present study, and not an AFP-assisted or any other adaptation. A smooth transition between adjacent frames is obtained by reducing the winding speed when the robot-eye enters a new frame. A friction coefficient of 0.3 between the filament and the steel-based mandrel was experimentally measured

The selected individuals to form a new solution (offspring) are selected following their fitness. The optimization converges for the following parameters: population of 50 individuals (more than 10 times the number of design variables), 50 generations, probability for mutation of 20%, and probability for crossover of 50% using a two-point crossover for reproduction of the next generation.

After all parameters for the GA are set, the optimization problem can be formulated as:

$$\text{Fitness function} \quad min \frac{1}{P_{cr}(\boldsymbol{\theta})}$$
$$\text{subject to}: \quad \boldsymbol{\theta}^L \leq \boldsymbol{\theta} \leq \boldsymbol{\theta}^U \tag{3}$$

where the fitness function goal is to maximize the first buckling load, P_{cr} (obtained by linear FE analysis - Section 2.2), and the design variables are $\boldsymbol{\theta}$, whose lower and upper bounds are represented by $\boldsymbol{\theta}^L$ and $\boldsymbol{\theta}^U$, respectively. The former is defined as the minimum winding angle to avoid fiber slippage for the current mandrel system [40], whereas the latter is defined by $\arccos(w/r) = 86.6°$, where w is the tow bandwidth and r is the mandrel radius.

To ensure a smooth winding angle transition between adjacent mandrel frames, preventing tow slippage, a maximum angle variation between consecutive control points (represented by dotted lines in Fig. 1) is set, being represented as:

$$|\theta_k - \theta_{k-1}| < 10° \tag{4}$$

in which k is a control point.

2.4. Optimization results

The optimization results are presented in Fig. 3, where the evolution of fitness is plotted against the generations. As can be seen, all three optimization cases are convergence-free and the global optimum for each case is certainly reached. The magnitude of the linear buckling loads follows the sequence VAFW8 > VAFW4 > CA.

The optimum winding angles for every cylinder is presented in Table 2, and the respective fiber paths are shown in Fig. 1. Fig. 1(a) shows the design with minimum winding angle (MA) and Fig. 1(b) shows the optimized design with constant angle (CA). The first VAFW optimization result for VAFW4 is illustrated in Fig. 1(c), showing a constant winding angle throughout the shell length, meaning that with only two design variables, that geometry and number of layers do not represent a design space large enough to generate a cylinder
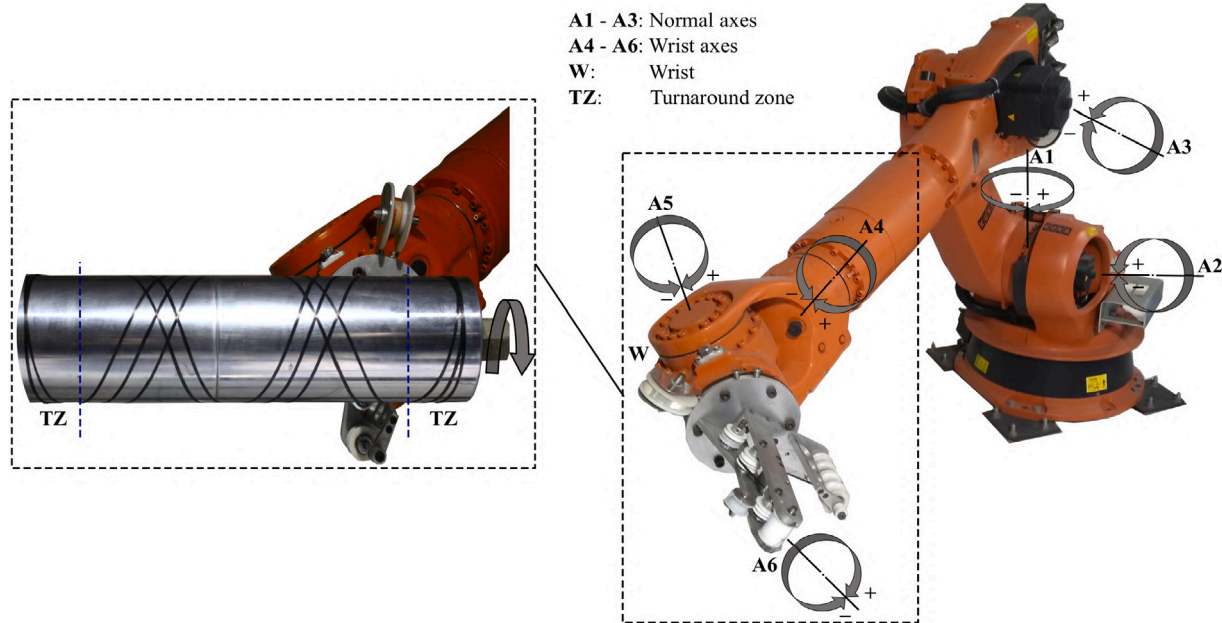
Fig. 4. The used Kuka robot and photograph of a VAFW8 cylinder being manufactured.
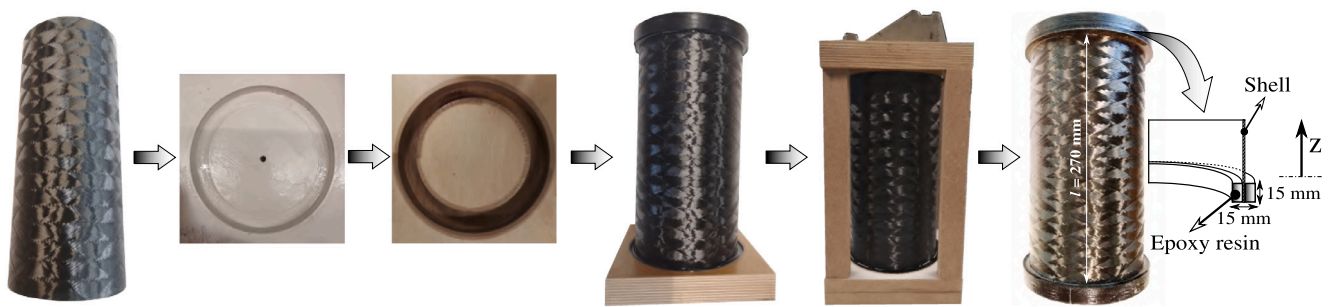

Fig. 5. Description of the casting procedure.

using the procedure detailed in Dalibor et al. [40]. A similar value for this material was also reported by Zu et al. [41]. Moreover, the robot has an angle tolerance of $\pm 0.15°$ in the deposition process, which is the tolerance control of the 7th axis.

The wrist axes, namely the rotating axes, are essential to minimize filament in-plane bending during deposition and aid, to some extent, in-plane shear on the filament. Therefore, the variable-angle is achieved through a combination of in-plane bending and shear, as described in Wang et al. [10]. Minimization of filament in-plane bending is achieved mainly by controlling and synchronizing the A4 wrist axis (see Fig. 4) to keep the filament as close as possible to the mandrel, which also prevents twisting. Here, the same winding pattern of 3/1 is used for all cylinders, minimizing the formation of gaps and overlaps [42]. Nevertheless, as shown in Table 3, it is not always possible to obtain a coverage of 100%, and a coverage as close as possible to 100% is chosen to prevent gaps, unavoidably leading to a thickness buildup in some areas. It is worth mentioning that neither fiber waviness nor wrinkles are observed in any of the manufactured cylinders.

3.2. Specimen preparation

Three cylinders of each design are manufactured, 12 in total. In order to enhance the load distribution around the specimen edge and prevent premature failure, a resin potting procedure is carried out using a metal-filled black-colored epoxy resin CW 2418-1 and hardener REN HY 5160 (100:15 ratio), both from Huntsman Corporation. The low-cost procedure consists of five steps, as per Fig. 5: (i) mold production; (ii) release agent application; (iii) casting one edge of the cylinder and curing for 16 h at room temperature; (iv) casting the other edge ensuring parallelism and curing for 16 h; and (v) removal of cylinder from the mold.

The molds are made of medium-density fiberboard (MDF), which are machined using a saw cup. After that, they are machined with cross-section dimensions of 15×15 mm, painted, and a release tape is applied onto the inner cavity. The upper mold is machined with four rectangular bars to aid alignment. Also, when the second potting is curing, a weight is placed on top of the mold (see Fig. 5) to ensure that the entire cylinder edge is in contact with the inner cavity of the mold. After curing, the whole mold apparatus can be easily removed and the cylinder is ready to be tested. Representative specimens are depicted in Fig. 6.

3.3. Testing

The cylinders herein investigated are subjected to axial compression. A Zwick Roell universal testing machine model LF7M19 with a load cell of 250 kN is used with compressive platens of 175 mm in diameter. The displacement-controlled tests are conducted at a rate of 1 mm/min.

The cylinders are painted to perform DIC measurements. The DIC is used to monitor both global displacements and strain field on about
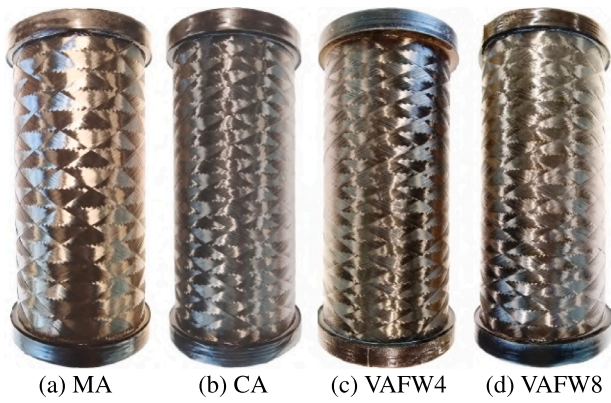
(a) MA   (b) CA   (c) VAFW4   (d) VAFW8

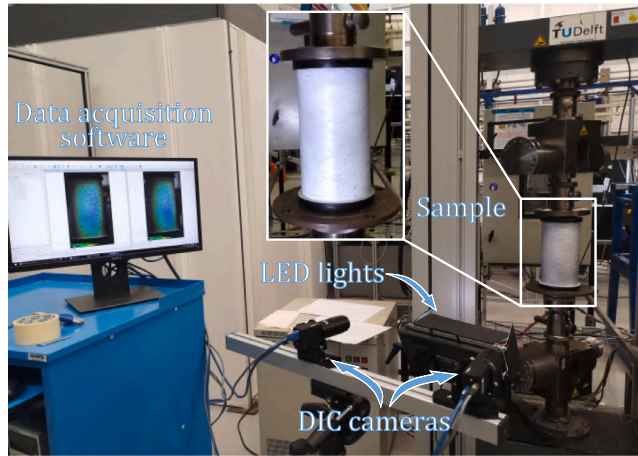**Fig. 6.** The prepared cylinders prior to testing.

Fig. 7. Axial compression test apparatus with the DIC system used for displacement and strain measurements during the tests.

60° of the cylinder's surface. During the deformation, the DIC tracks the gray value pattern in small neighborhoods called subsets. The calibration of the DIC system is performed before testing each cylinder, with the specimen compressed at a preload of 200 N, which is sufficient to remove slack from all force–displacement curves. This strategy also plays a key role in stabilizing and aligning the sample between the compressive platens. Fig. 7 schematically depicts the experimental setup. In this study, two 9 megapixel cameras with 50 mm lenses are used.

3.4. Variable thickness patterns

Before the compression tests, the surface topography of all cylinders is measured using the same DIC system. Castro et al. [32] describe in detail the algorithm to do the thickness imperfection measurement using data from only one pair of cameras. In brief, the procedure consists in collecting DIC raw data from 6 circumferential positions along the cylindrical shell and transforming them to a common reference frame. Next, the raw data is rotated to the position of the corresponding section, with a fine adjustment based on mean-squared value error. Once all sections are reconstructed, the surface topography can be precisely determined by knowing that the outer surface of the mandrel is smooth. These measured imperfections are afterwards imprinted in nonlinear FE models (see Section 4) to reproduce the imperfect geometries.

The stitched imperfection patterns adopted for each VAFW cylinder are shown in Fig. 8. The raw DIC data [43] and reconstructed three-dimensional imperfection data [44] are available for public access.

3.5. Experimental results

After obtaining substantial improvement in terms of buckling load from the optimization process, both non-optimized and optimized cylinders are manufactured and tested. The experimental load-shortening curves are shown in Fig. 9 (Section 5), where three samples are tested for each family of cylinder. Generally speaking, there is a very good repeatability, as expected from an automated process such as filament winding. The designed cylinders VAFW8 have clearly more deviation on stiffness and failure load. For the non-optimized baseline MA cylinder (Fig. 9(a)), all three specimens present negligible variation in terms of stiffness. Specimen MA–3 has a greater failure load, but its axial stiffness is similar to the other two MA samples. As given in Table 5, the MA design has an axial stiffness of 5.8 ± 0.1 kN/mm, and a failure load of 11.8 ± 1.4 kN. Fig. 9(b) presents the test results for the cylinder CA, showing an average stiffness of 5.9 ± 0.4 kN/mm and failure load of 12.5 ± 0.8 kN. Fig. 9(c) shows the load–displacement curves for the VAFW4 cylinder, with stiffness of 6.4 ± 0.4 kN/mm and failure load of 13.5 ± 1.1 kN. The optimized VAFW8 cylinders (9(d)) have the highest stiffness (8.5 ± 1.4 kN/mm) and failure load (20.5 ± 3.8 kN) among all designs. The results for the VAFW8 cylinder show the great potential of the proposed VAFW designs to improve the mechanical performance of cylindrical shells. This family of cylinders shows, nonetheless, higher variations compared to the other cylinder designs, which can be attributed to possible small angle variations at the control points areas. In addition, the large number of frames along the axial direction of the cylinder can yield several transitions between frames, whose zones might show a small tow angle deviation.

The axial compression tests are assisted by DIC and these results are presented in Figs. 10, 11, 12, 13, which are the displacement and strain fields for the specimens MA–1, CA–2, VAFW4–3, and VAFW8–1, respectively (it is insightful to correlate these results with the load–displacement curves given in Fig. 9. Three load levels are captured and shown in these Figures, namely before failure (pre-failure), at the maximum compressive load (failure), and post-failure. The characteristics of each cylinder is next described in detail:

MA cylinder (Fig. 10):

- U_z: the distribution of axial displacement is fairly stable in the linear region, i.e., at the pre-failure region. Subsequently, there is a non-linear regime as the cylinder approaches the bifurcation point. The cylinder buckles near the top edge as evidenced by the large shortening area in purple.
- U_r: Similarly to the axial displacement, the radial displacement maintains a consistent profile throughout the linear regime of the test. There is a high level of out-of-plane displacement along the cylinder length, which starts near the edge of the shell. At the maximum load, the structure buckles near the top edge. After failure happens, the shell finds itself into a deep post-buckling state, in which a crack along the tow direction is observed followed by a pronounced localized buckle.
- ϵ_{zz}: the axial strain provides very useful information since the winding pattern can be clearly seen, both global strain field and local strain concentrations can be identified, which helps understanding how the shell responds to the axially compressive load. At initial load levels, strain concentrations are observed near the edges and along the tows, that is, at the helical cross-over zone (see winding pattern explanations in [42]). At pre-failure plot, which is taken just prior failure, the strain localizes at the top, near the buckling zone. From these strain field maps, the helical zones create a local strain concentration and can be seen as imperfections on the VAFW cylinders. The effect of these imperfections together with the measured thickness pattern are discussed next.
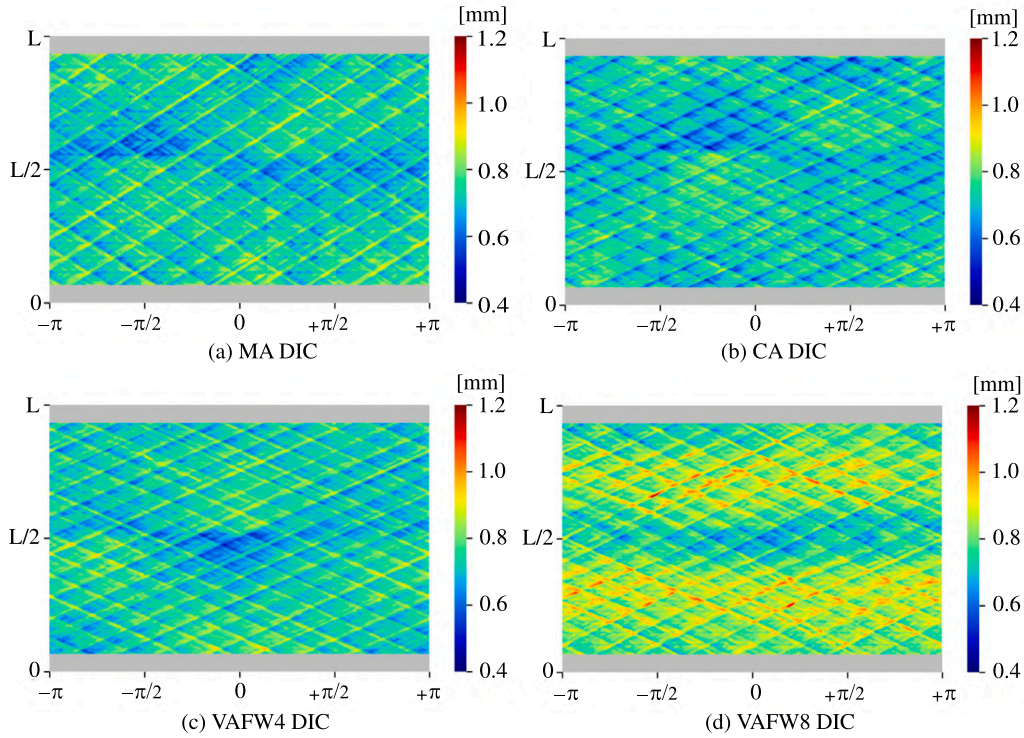
Fig. 8. Experimentally-measured geometric (thickness) imperfection patterns [32]. The gray areas represent the edges with resin potting. (For interpretation of the references to color in this figure legend, the reader is referred to the web version of this article.)

- ϵ_{eq}: the equivalent strain map, calculated from the principal strains ϵ_1 and ϵ_2 as $\epsilon_{eq} = \sqrt{\epsilon_1^2 - \epsilon_1\epsilon_2 + \epsilon_2^2}$, reveals that stresses tend to concentrate around imperfections. At the pre-failure, two pronounced strain concentration areas can be clearly seen at two tow segments near the bottom and top edges (see red areas), which makes the cylinder prone to suddenly buckle in those areas. Then, a strong strain concentration is seen along the buckled area around the top edge.

Most of the observations made for the MA cylinders also apply to the **CA design** since they both have constant-angle configurations. Nevertheless, **cylinder CA** (Fig. 11) shows strong evidences of material failure instead of buckling. Besides, it should be noted that:

- U_z: similar and expected axial displacement prior to failure, varying linearly from top to the bottom of the sample, with a change in form at failure and at post-failure, that is, when the shell is not able to sustain any load anymore, characterized by higher displacement level towards the failure location near the lower edge.
- U_r: the radial displacement varies very slightly around the circumference of the cylinder and reaches maximum levels around the shell mid-length. At failure, a higher radial displacement is found near the main crack. A similar scenario is identified at the post-failure.
- ϵ_{zz}: higher deformation at the helical cross-over imperfection areas and around the edges. At failure, the axial strain concentrates at the lower edge of the specimen, location where the cylinder fails.
- ϵ_{eq}: stresses concentrate along the imperfections, but with higher magnitude near the lower edge mainly due to the contribution of transverse strain ϵ_2.

Given that the optimization for the **VAFW4 cylinder** also provides a constant-angle fiber path, similar interpretations are inferred (Fig. 12):

- U_z: the axial shortening is as expected, in which a change is only observed after the structure buckles closer to the cylinder mid-length.
- U_r: the radial displacement is also very similar, with higher radial (out-of-plane) displacement levels along the shell length. The level of radial displacement for this cylinder is about 20% of the axial displacement. This behavior is better captured with reduced integration shell elements, as utilized here, once elements with full integration might undergo shear and membrane locking and, therefore, the finite elements would be too rigid and certainly these levels of radial displacement would not be captured.
- ϵ_{zz}: the same observations are made here, where thickness imperfections create strain concentrations more prone to buckle than the "regular laminate" areas, i.e., the diamond-shapes formed during manufacturing.
- ϵ_{eq}: at pre-failure, this strain field is has some strain concentrations around the upper and lower edge mainly due to the contribution of transverse strain. At failure, this strain is considerably high at the cylinder mid-length at the local dimple. The post-failure equivalent strain field is very similar to the one at failure, which characterizes a short post-buckling range.

The design **VAFW8** (Fig. 13) has a VAFW configuration and a different failure mode, i.e. material failure instead of buckling. Further observations are as follows:

- U_z: the axial displacement before failure varies linearly from the upper edge towards the lower one, similarly to the other designs. At failure, large axial displacement levels are seen at the lower edge, where the main crack is located.
- U_r: the radial displacement colored map shows a uniform radial displacement. An interesting characteristic is that the radial displacement is higher at the specimen ends. The development of membrane stresses after failure suggests a retention of axial stiffness, which can be qualitatively verified at the post-failure region. Differently than the other family of cylinders, neither dimple nor other buckling evidences are identified for this sample,
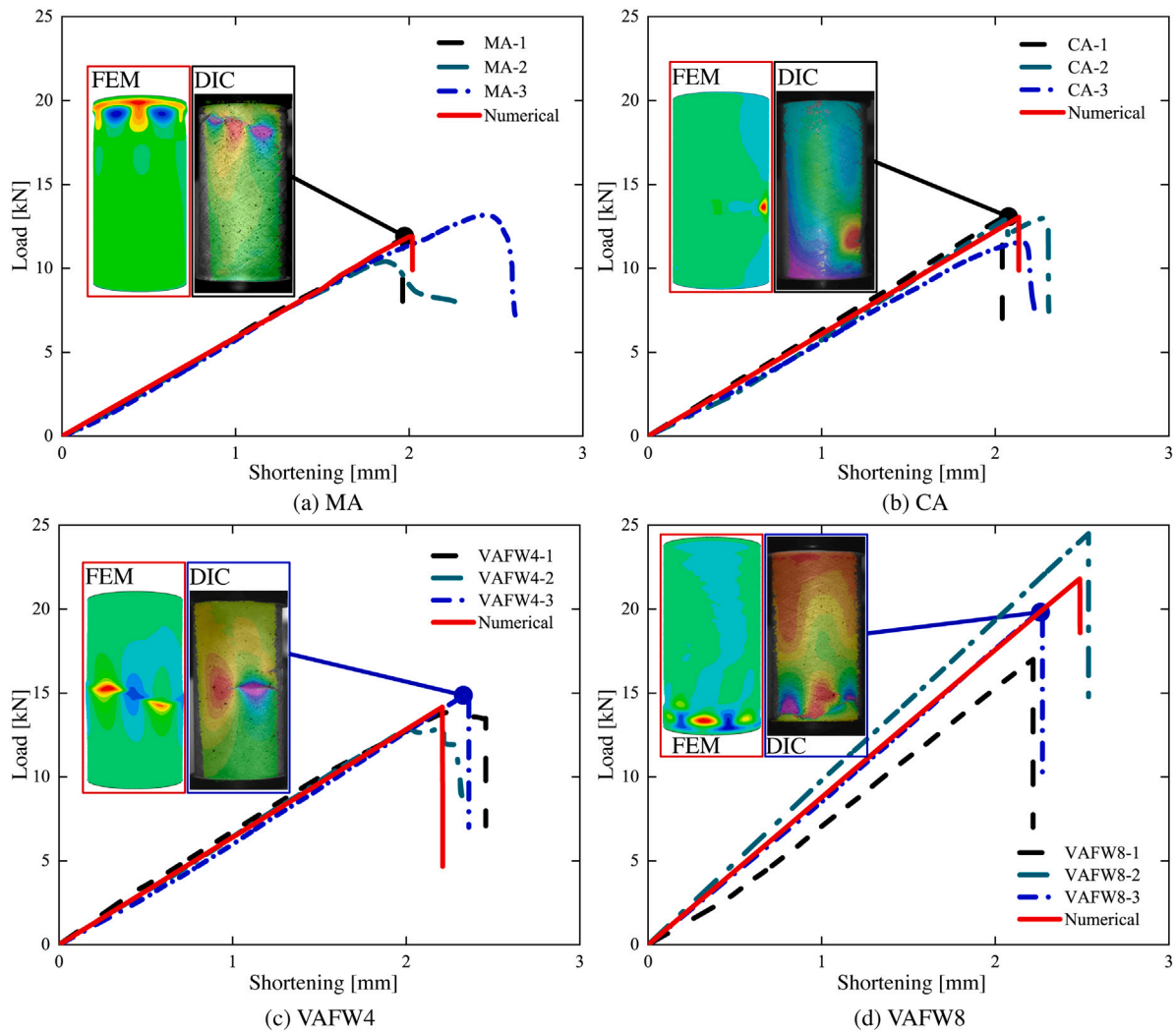
Fig. 9. Experimental and numerical load–displacement curves for all cylinders. The plots inside each frame represent the radial displacement field (U_r) from FEM and DIC at the failure (maximum) load. (For interpretation of the references to color in this figure legend, the reader is referred to the web version of this article.)

confirming that any of the material strengths are reached and therefore the cylinders fails by material failure.

- ϵ_{zz}: although the axial strain has a similar characteristic, that is, higher strain concentrations in thickness-imperfection areas, the magnitude of the deformations is lower up to 12 kN. Interestingly, after this point, the "regular laminate" areas (diamond-shaped regions) show substantial axial strain accumulation when approaching the failure load. This can be explained by the thickness build-up, which is necessary to produce this configuration of cylinder, as can be seen in Figs. 6(d) and 1(d). A large and pronounced crack along with high levels of axial strain is observed near the lower edge of the cylinder, confirming that buckling is postponed with the optimization at a sufficient level that the structure fails by transverse compression instead of experiencing structural instability.

- ϵ_{eq}: the equivalent strain maps are similar to the ϵ_{zz} fields, in which when the shell approaches the failure load, there is a load alleviation in the thicker areas and higher deformation within the diamonds. The final failure occurs near the bottom end with a major crack along the tow direction.

The thickness imperfection patterns of Fig. 8 can be used together with the displacement and strain maps of Figs. 10–13 to better understand the failure mechanism of the FW cylinders. The regions with higher localized thickness are the helical cross-over zones. Looking at

the axial strains (ϵ_{zz}) at compression loads near the onset of failure and comparing with the out-of-plane displacement (W) after failure, show that the failure appear near the helical cross-over zones. This result supports the previous remark that the helical cross-over zones have lower strain, and now this lower strain can be attributed to a self-stiffened region with a well-defined tow overlap pattern, which is crucial to postpone buckling occurrence. The combination of optimum winding angles for the cylinder VAFW8 with the generated tow overlapping necessary to make the winding kinematically possible [10] are the main structural features and design parameters of the VAFW cylinders to achieve a tailored stiffness and axial compressive performance. During the design of VAFW cylinders one should also focus on optimizing the tow overlapping patterns in order to delay the strain concentration that triggered the buckling, avoiding geometrically nonlinear degradation of the shell in-plane stiffness [45]. This nonlinear stiffness degradation in cylinders is very pronounced when the imperfection pattern is oriented circumferentially, as in the case of axisymmetric imperfections [46].

4. Nonlinear FE modeling

After the design and optimization (Section 2, the cylinders are manufactured and tested, as shown in Section 3, in which the geometric imperfections of manufactured cylinders are also presented. At this point, in order to properly simulate the experimental results, nonlinear FE models are built including the geometric imperfections of the
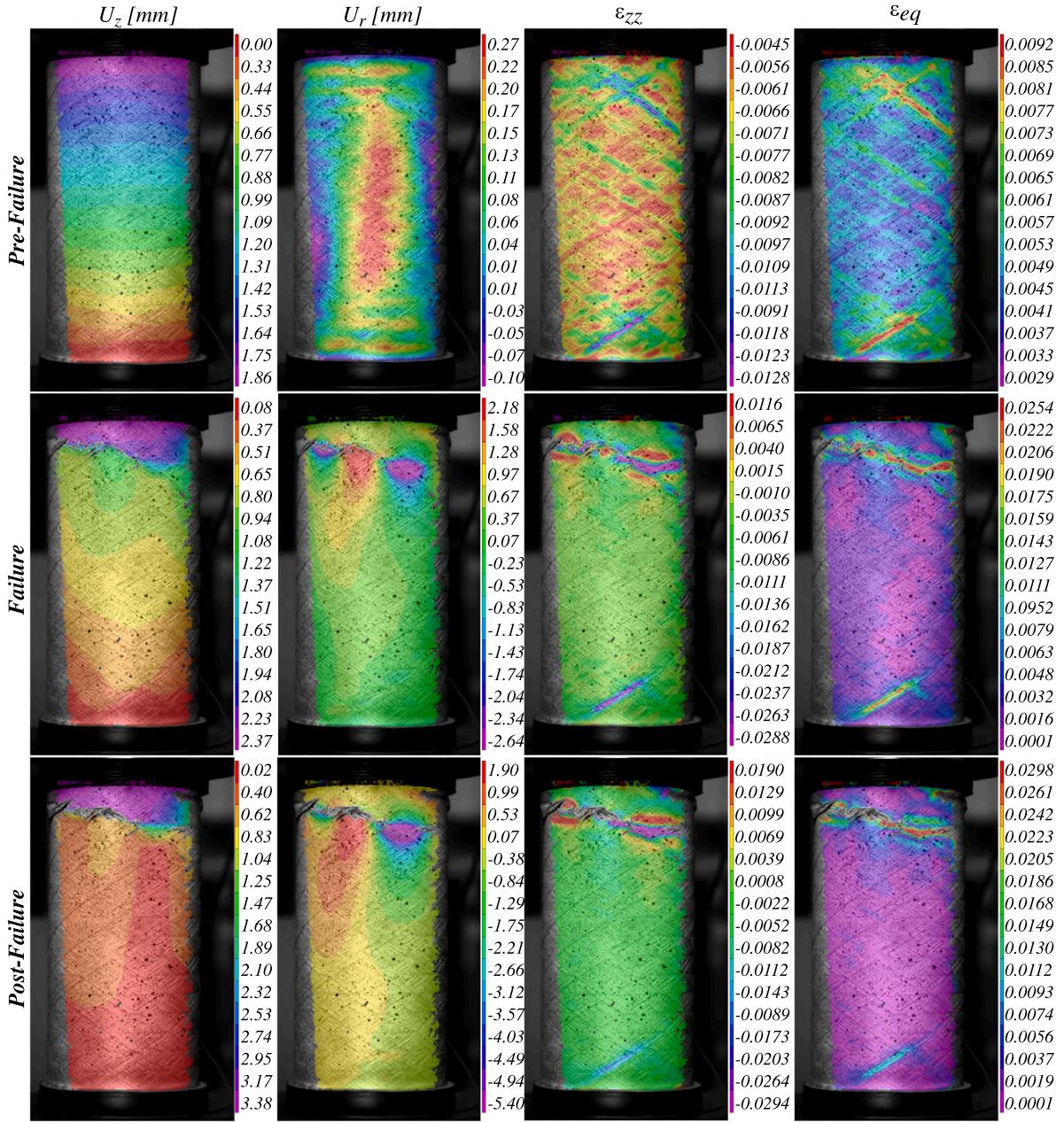
Fig. 10. Experimental color-maps from DIC for the MA cylinder just prior to fail, at the failure (maximum load), and post-failure: axial displacement U_z, radial displacement U_r, axial strain ϵ_{zz}, and equivalent strain ϵ_{eq}. (For interpretation of the references to color in this figure legend, the reader is referred to the web version of this article.)

manufactured cylinders and a progressive damage model, explained next. For all subsequent static analyses, a Newton–Raphson solver with adaptive time increments stabilized by artificial damping is used to solve the nonlinear problem. The following parameters are used for all simulations: initial increment size of 10^{-4}, minimum increment of 10^{-15}, maximum number of 1000 increments, and artificial damping factor of 2×10^{-5}.

4.1. Geometric imperfections

The manufacturing process of the current VAFW leads to a smooth inner surface of the cylindrical shells, such that all the thickness buildup occurs at the outer surface, resulting in a combination of mid-surface imperfection (MSI) and thickness imperfection (TI). These two geometric imperfections are imprinted into the nonlinear FE model using the procedure explained in Castro et al. [46], using the DESICOS plug-in

for Abaqus [47]. The thickness buildup is applied assuming that the stacking sequence is unchanged by scaling up the thickness of each ply to match the thickness of the measured imperfection patterns, such that the local fiber orientation is maintained. Fig. 14 shows the geometric imperfections of Fig. 8 imprinted on the FE models.

The thickness value is calculated per element, using the centroid of the element $\boldsymbol{x}_e = x_e, y_e, z_e$ as a reference coordinate to calculate the interpolated imperfections. The interpolation starts by discretely mapping the measured thickness imperfection h_i in the 3D Cartesian space to achieve $h_i(\boldsymbol{x}_i)$, with the components of $\boldsymbol{x}_i = x_i, y_i, z_i$ defined as:

$$
\begin{aligned}
x_i &= R \cos \theta_i \\
y_i &= R \sin \theta_i \\
z_i &= z_i
\end{aligned}
\tag{5}
$$

where R is the nominal radius of the cylinders, and θ_i, z_i are the cylindrical coordinates for which the measured imperfections are mapped.
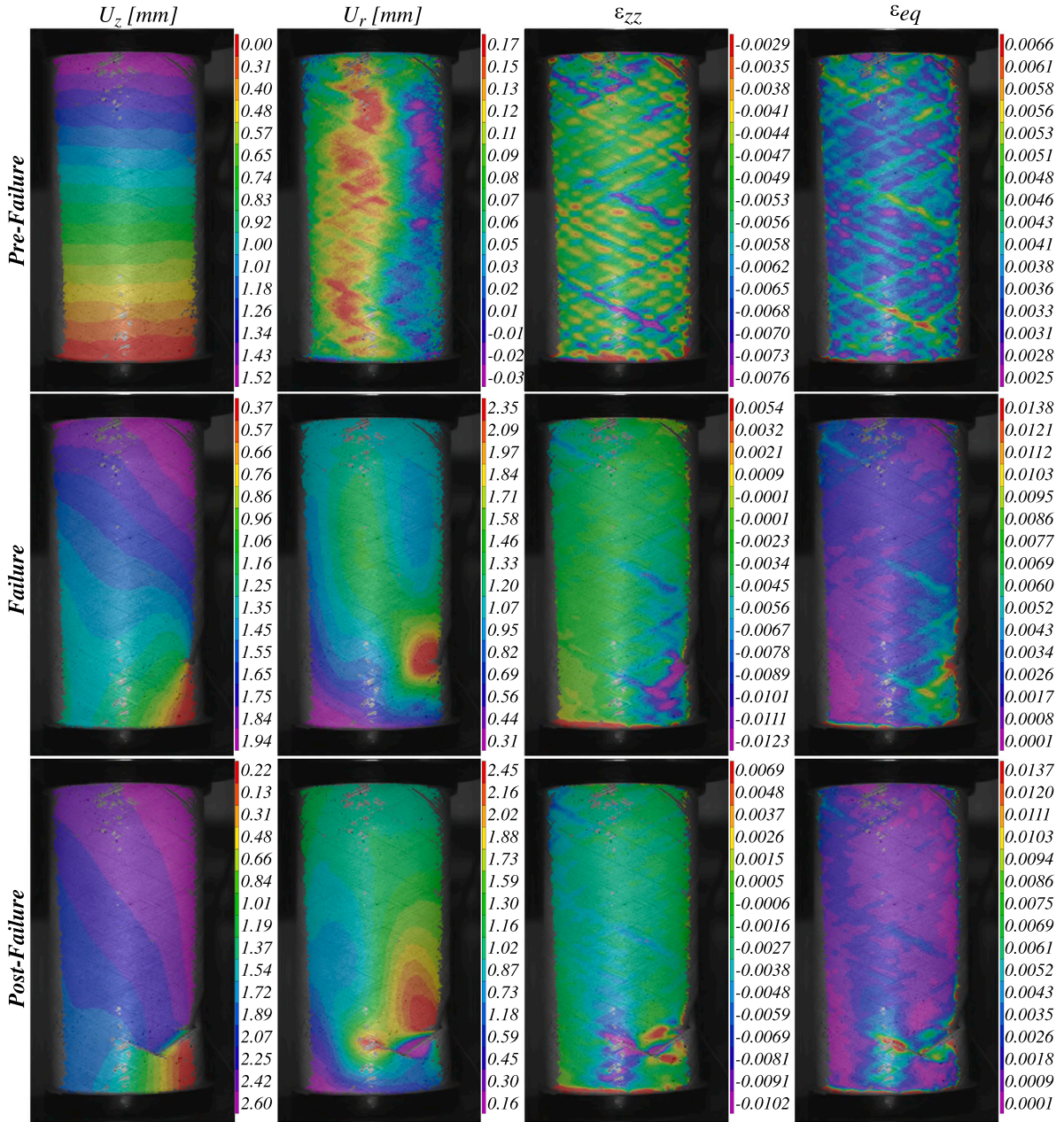
Fig. 11. Experimental color-maps from DIC for the CA cylinder just prior to fail, at the failure (maximum load), and post-failure for: axial displacement U_z, radial displacement U_r, axial strain ϵ_{zz}, and equivalent strain ϵ_{eq}. (For interpretation of the references to color in this figure legend, the reader is referred to the web version of this article.)

Next, the imperfections of the n closest measurement points are assigned to each element using:

$$h_e(x_e, y_e, z_e) = \sum_{i=1}^{n} w_i h_i(x_i, y_i, z_i) \tag{6}$$

where w_i is an inverse-weighting factor, calculated as:

$$w_i = \frac{\frac{1}{d(x_i - x_e)}}{\sum_{i=1}^{n} \frac{1}{d(x_i - x_e)}} \tag{7}$$

with the function $d(x_i - x_e)$ giving the distance between the measured points x_i and the element centroid x_e.

4.2. Progressive damage analysis

Once imperfections are implemented into the CAE environment, a progressive damage analysis is performed. This nonlinear FE simulation predicts the load–displacement response of the cylinders and provides insights on both damage initiation and propagation. Therefore, these analyses are essential to identify the failure mode of the cylinders, that is, whether the structures fail by material failure or buckling.

The boundary conditions used in the nonlinear FE simulations (which include geometric imperfections) are similar to those used in linear FE predictions. Nevertheless, the buckle step analysis is replaced by a static one in which an axial compressive displacement is applied to the top nodes (controlled by reference point 1, $RP1$ – Fig. 2). Then, the reaction force of $RP1$ is traced throughout the simulations.

Hashin failure criterion [48] is used to predict damage initiation, in which four damage initiation mechanisms are considered: fiber tension, matrix tension, fiber compression, and matrix compression. An overview of the damage initiation criteria is presented in Table 4.
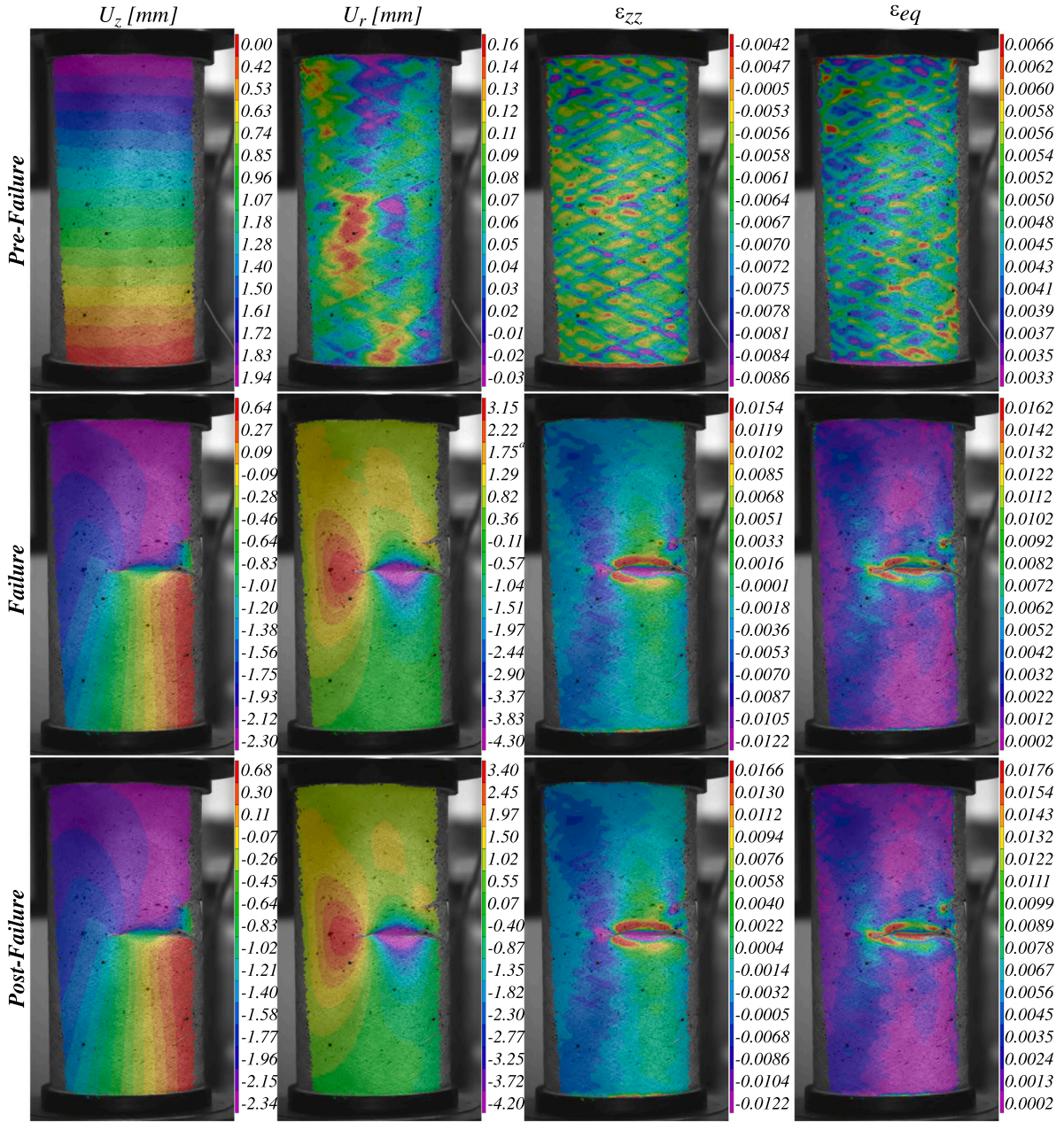
Fig. 12. Experimental color-maps from DIC for the VAFW4 cylinder just prior to fail, at the failure (maximum load), and post-failure for: axial displacement U_z, radial displacement U_r, axial strain ϵ_{zz}, and equivalent strain ϵ_{eq}. (For interpretation of the references to color in this figure legend, the reader is referred to the web version of this article.)

Table 4
Failure criteria and damage evolution laws for each failure mode.

Failure type	Failure criteria	Damage propagation laws	
		Equivalent displacement	Equivalent stress
Longitudinal tension ($\hat{\sigma}_{11} \geq 0$)	$(\hat{\sigma}_{11}/X_T)^2 + \alpha(\hat{\tau}_{12}/S_L)^2$	$\delta_{eq}^{ft} = L^c\sqrt{\langle\varepsilon_{11}\rangle^2 + \alpha\varepsilon_{12}^2}$	$\sigma_{eq}^{ft} = \frac{\langle\sigma_{11}\rangle\langle\varepsilon_{11}\rangle + \alpha\tau_{12}\varepsilon_{12}}{\delta_{eq}^{ft}/L^c}$
Longitudinal compression ($\hat{\sigma}_{11} < 0$)	$(\hat{\sigma}_{11}/X_C)^2$	$\delta_{eq}^{fc} = L^c\langle-\varepsilon_{11}\rangle$	$\sigma_{eq}^{fc} = \frac{\langle-\sigma_{11}\rangle\langle-\varepsilon_{11}\rangle}{\delta_{eq}^{fc}/L^c}$
Matrix tension ($\hat{\sigma}_{22} \geq 0$)	$(\hat{\sigma}_{22}/Y_T)^2 + (\hat{\tau}_{12}/S_L)^2$	$\delta_{eq}^{mt} = L^c\sqrt{\langle\varepsilon_{22}\rangle^2 + \varepsilon_{12}^2}$	$\sigma_{eq}^{mt} = \frac{\langle\sigma_{22}\rangle\langle\varepsilon_{22}\rangle + \tau_{12}\varepsilon_{12}}{\delta_{eq}^{mt}/L^c}$
Matrix compression ($\hat{\sigma}_{22} < 0$)	$[(Y_C/2S_T)^2 - 1](\hat{\sigma}_{22}/Y_C)$ $+(\hat{\sigma}_{22}/S_T)^2 + (\tau_{12}/S_L)^2$	$\delta_{eq}^{mc} = L^c\sqrt{\langle-\varepsilon_{22}\rangle^2 + \varepsilon_{12}^2}$	$\sigma_{eq}^{mc} = \frac{\langle-\sigma_{22}\rangle\langle-\varepsilon_{22}\rangle + \tau_{12}\varepsilon_{12}}{\delta_{eq}^{mc}/L^c}$

α: coefficient to determine the contribution of shear stress to fiber tensile criterion.
L^C: characteristic length computed as the square root of the finite element surface area.

All failure criteria are checked in every step along the simulation through the effective stress tensors, $\hat{\sigma}$, which are computed from:

$$\hat{\sigma} = \mathbf{M}\sigma \tag{8}$$

in which σ is the nominal stress and $\mathbf{M}$ is the damage tensor. The approach proposed by Matzenmiller et al. [49] is used to compute the degradation of the stiffness matrix. Prior to any damage initiation, $\mathbf{M}$
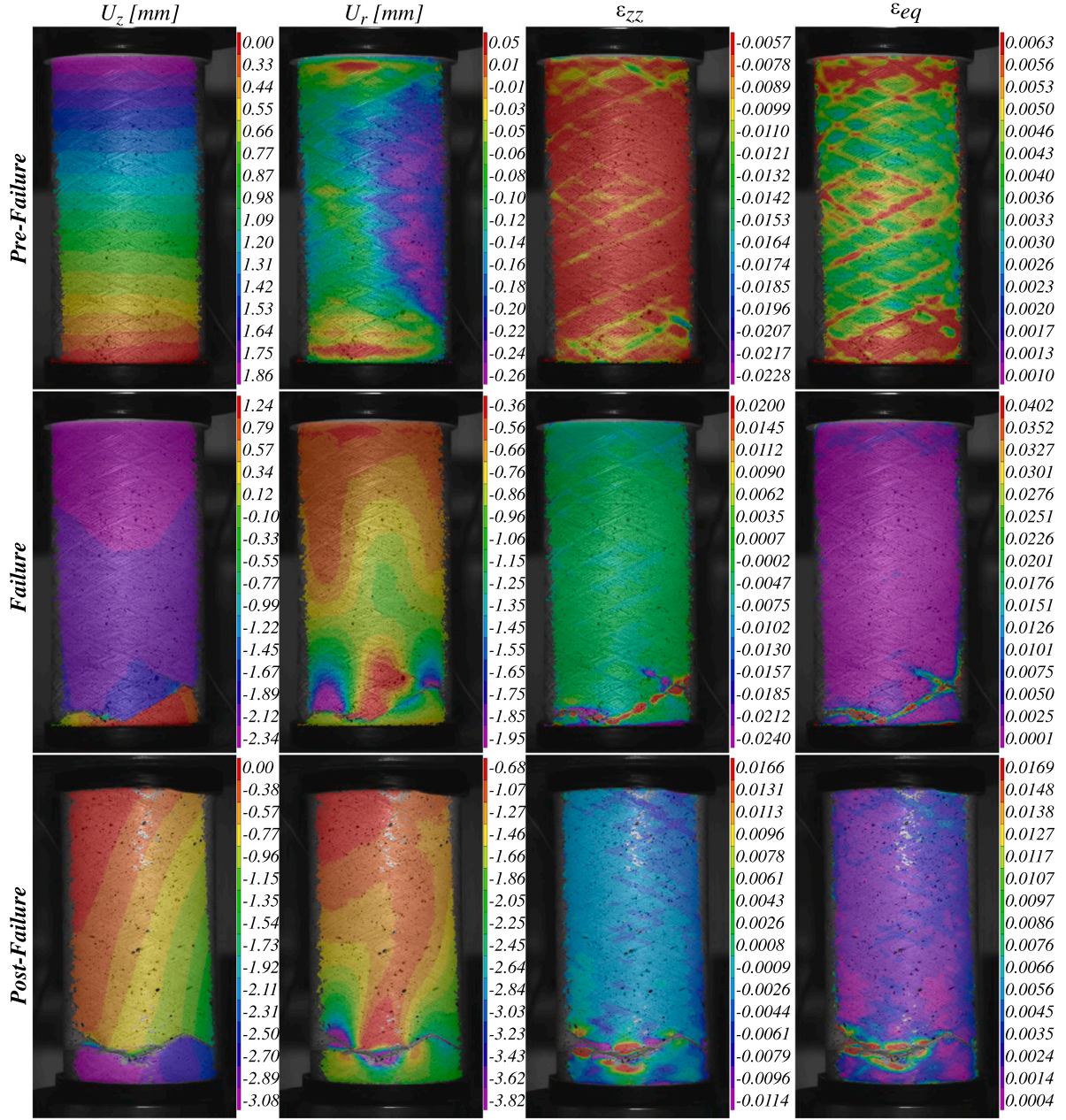
Fig. 13. Experimental color-maps from DIC for the VAFW8 cylinder just prior to fail, at the failure (maximum load), and post-failure for: axial displacement U_z, radial displacement U_r, axial strain ϵ_{zz}, and equivalent strain ϵ_{eq}. (For interpretation of the references to color in this figure legend, the reader is referred to the web version of this article.)

is equal to the identity matrix, thus $\hat{\sigma} = \sigma$. Then, **M**, which is written in Voigt notation, is given by

$$
\mathbf{M} = \begin{bmatrix} \dfrac{1}{1-d_F} & 0 & 0 \\ 0 & \dfrac{1}{1-d_M} & 0 \\ 0 & 0 & \dfrac{1}{1-d_S} \end{bmatrix}
\tag{9}
$$

where d_F, d_M, and d_S are fiber, matrix and shear internal damage variables defined by

$$
d_F = \begin{cases} d_{ft} & \hat{\sigma}_{11} \geq 0 \\ d_{fc} & \hat{\sigma}_{11} < 0 \end{cases} \qquad d_M = \begin{cases} d_{mt} & \hat{\sigma}_{22} \geq 0 \\ d_{mc} & \hat{\sigma}_{22} < 0 \end{cases}
$$
$$
d_S = 1 - \left(1 - d_F^T\right)\left(1 - d_F^C\right)\left(1 - d_M^T\right)\left(1 - d_M^C\right)
\tag{10}
$$

where d_F^T, d_F^C, d_M^T, and d_M^C are damage indices associated to fiber tensile, fiber compression, matrix tensile, and matrix compression failure, respectively.

Once any of the four damage initiation criteria is met, any further loading causes degradation of the stiffness matrix. Thenceforth, the damaged stiffness matrix **D** is given by

$$
\hat{\sigma} = \mathbf{D}\epsilon
\tag{11}
$$

in which ϵ is the strain and **D** is given by

$$
\mathbf{D} = \frac{1}{K} \begin{bmatrix} (1-d_F)E_1 & (1-d_F)(1-d_M)\nu_{21}E_1 & 0 \\ (1-d_F)(1-d_M)\nu_{12}E_2 & (1-d_M)E_2 & 0 \\ 0 & 0 & (1-d_s)G_{12}K \end{bmatrix}
\tag{12}
$$

where $K = 1 - (1-d_F)(1-d_M)\nu_{12}\nu_{21}$.

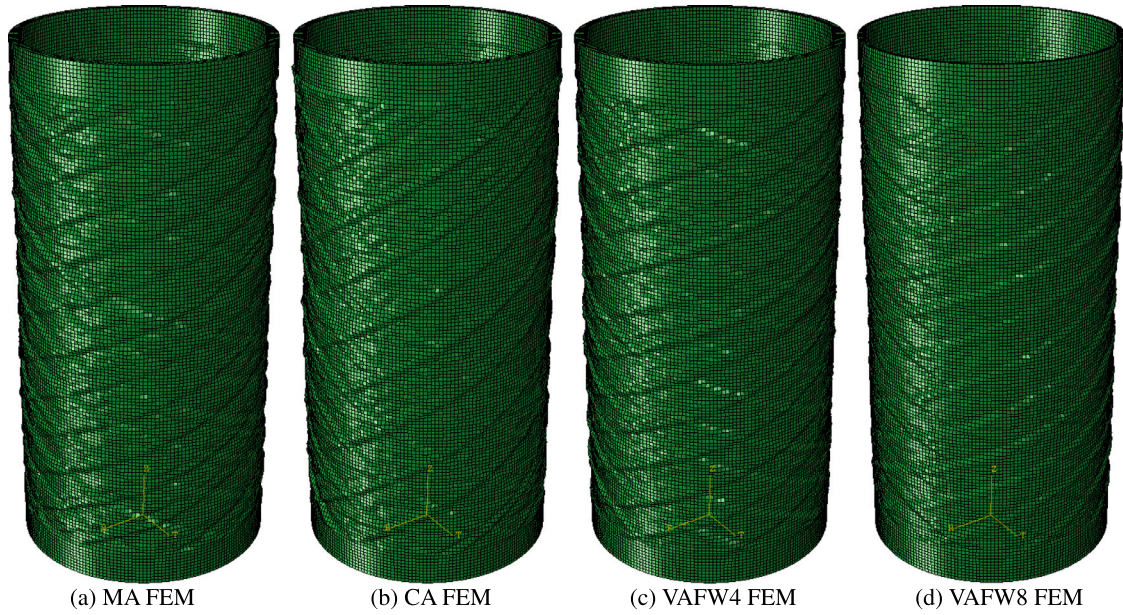|			
(a) MA FEM	(b) CA FEM	(c) VAFW4 FEM	(d) VAFW8 FEM

Fig. 14. Experimentally-measured imperfection patterns implemented into the FE models. For visualization purposes, a magnification factor of 3X is used here.

The evolution of each damage variable is governed by an equivalent displacement, δ_{eq}, where δ_{eq} for each mode is expressed in terms of equivalent stress components σ_{eq}. The equivalent displacement and stress for all four modes are presented in Table 4. For each failure mode, the damage indices drive the stiffness reduction and have values between 0 (undamaged) and 1 (damaged). The damage index for each mode is then derived through the following relation:

$$d = \frac{\delta_{eq}^f \left(\delta_{eq} - \delta_{eq}^0 \right)}{\delta_{eq} \left(\delta_{eq}^f - \delta_{eq}^0 \right)} \tag{13}$$

in which δ_{eq}^0 is the equivalent displacement when a particular damage initiation criterion is satisfied and δ_{eq}^f is the displacement when the material is fully damaged in a damage mode.

4.3. Numerical results

Fig. 9 (Section 5 – see red curves) presents the predicted load-shortening curves from the progressive damage analysis of imperfect cylinders. It is observed an increase in terms of both stiffness and strength in the same order observed experimentally: VAFW8 > VAFW4 > CA > MA. The shape of the curves is also similar, i.e., nearly linear-elastic followed by abrupt failure after the critical load is reached.

The nonlinear FE simulations are used to identify the first failure mode of each cylinder, either buckling or material failure. The damage indices defined in Section 2.2 (d_F^T, d_F^C, d_M^T, d_M^C) are monitored throughout the simulations, and it is assumed that material failure occurs if any damage index exceeds 1.0. However, if there is a drop in reaction load and all damage indices are below unity, it is assumed that buckling occurs first.

Fig. 15 depicts the damage index for all simulations. None of the failure indices for cylinders MA and VAFW4 reach 1.0 (only d_F^C is triggered, but far below a failure index of 1.0). However, cylinders CA and VAFW8 reach a failure index of 1.0 after the critical load is reached. In other words, all cylinders buckle but only cylinders CA and VAFW8 present a post-buckling range that is sufficient to trigger a subsequent material failure. Assessing the damage indices for design CA, damage initiates by matrix tension, followed by matrix compression, and then fiber tension is triggered later, as shows Fig. 15(b). Only d_M^C index, nevertheless, reaches a value of 1.0. For cylinder VAFW8, it can be noted that damage is triggered by matrix tension, followed by matrix

compression. Differently than for CA, notwithstanding, both fiber tension and fiber compression damage indices are triggered and strongly contribute to the final collapse, as depicted in Fig. 15(d).

The highest damage index for every cylinder is plotted in Fig. 16. Analogously to Fig. 15, the highest index is matrix compression d_F^C for cylinders MA and VAFW4, and d_M^C for cylinders CA and VAFW8. These plots confirm that cylinders MA and VAFW4 fail by buckling, whereas CA and VAFW8 fail by material failure, in which the main mechanism is matrix compression. For the cylinder VAFW8, large and pronounced cracks along the fiber direction are observed, in which damage initiates at the thickness transition areas and rapidly propagates along the tow direction throughout the cross-over zones. The VAFW8 is a interesting example of an effective use of variable-stiffness structures, in this case able to postpone buckling and allow the structure to reach the material strength limits, instead of losing the structural integrity prematurely by buckling. The VAFW8 also reached the highest compressive strength without the need of adding extra layers.

5. Discussion

The experimental results and numerical predictions for each family of cylinder are included in Fig. 9. In these nonlinear FE models, the geometric imperfections shown in Fig. 14 are taken into account. For the four designs, the simulations can represent well the experimentally observed stiffness and failure load. The consideration of experimentally-measured geometric imperfections and a proper progressive damage model are essential to generate accurate predictions using the nonlinear FE model.

Fig. 9 also includes the radial displacement field U_r at the maximum compressive load obtained numerically and experimentally using DIC. In general, there is a good agreement between the FE model and the DIC for all cylinders, where the following aspects are observed for each design:

MA: Fig. 9(a) shows that the predicted U_r is located slightly lower than the experimental one. The FE plot also reveals that the MA cylinder starts concentrating stress near the top edge of the cylinder (see darker red areas), just like in the experiments, and it buckles locally generating a local dimple.

CA: Fig. 9(b) shows a material failure pattern. Although the FE plot shows a vestige of buckling near the cylinder mid-length, there are high levels of radial displacement around the cylinder length (see lighter red
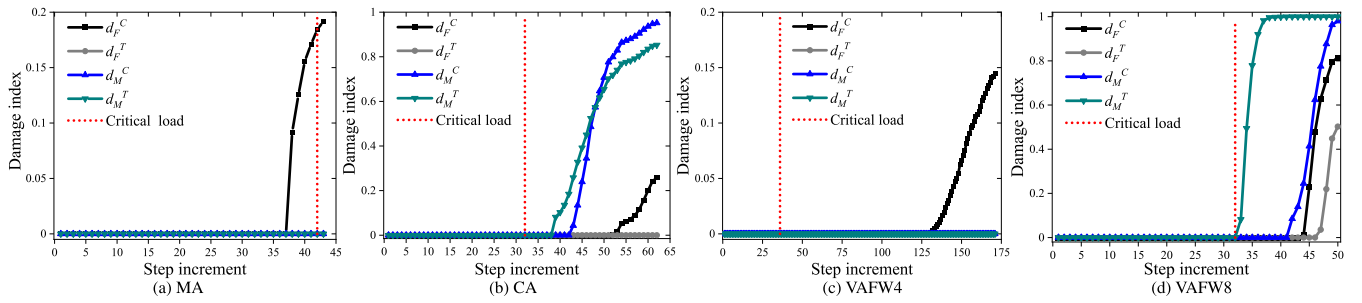
Fig. 15. Monitoring of all four damage indices throughout the simulations for every cylinder.
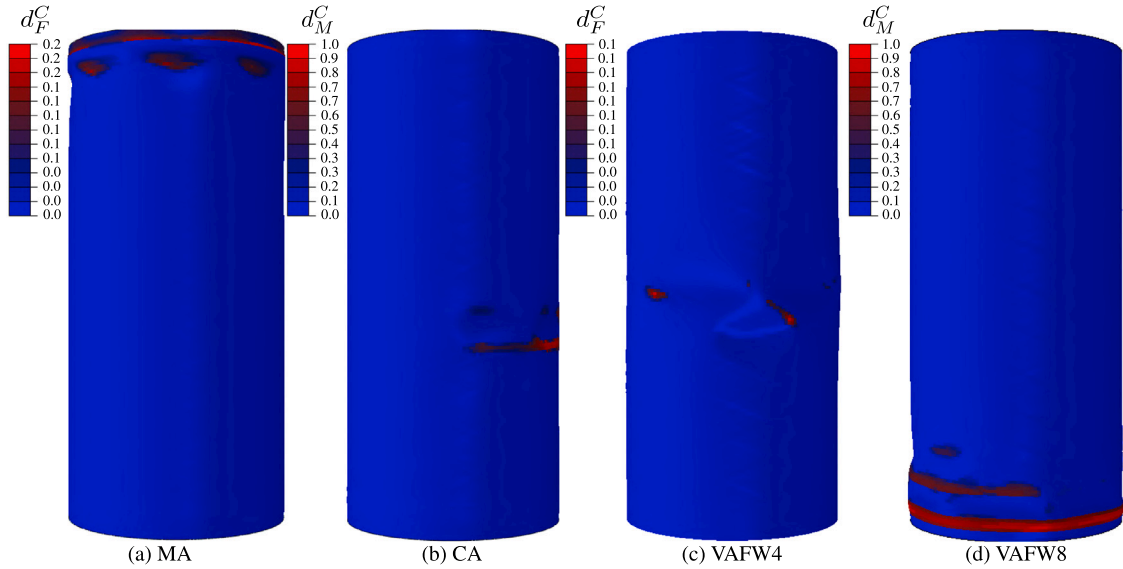

Fig. 16. Plot of the most critical damage mode after failure for every cylinder. (For interpretation of the references to color in this figure legend, the reader is referred to the web version of this article.)

areas), which concentrate stress and is mainly dominated by matrix compression. The DIC pattern shows high radial displacement at the lower part of the cylinder, and it should be pointed out that evidences of buckling were found at the backside of the area covered by the DIC cameras, therefore not shown here.

VAFW4: These simulated and experimental patterns (Fig. 9(c)) are similar in terms of location and mode. Two major dimples are seen in the middle of the cylinder, but with different displacement magnitudes. The greater dimples are shown in both cylinders in blue, whereas the less-pronounced one are seen in light red in the FE pattern, and in red in the DIC pattern.

VAFW8: FE and DIC U_r fields for this cylinder (Fig. 9(d)) are in reasonable agreement. The failure pattern of this design strongly differs from the other three cylinders. Looking at the numerical U_r field, there is a large and pronounced crack along the fiber direction, which begins at the cylinder mid-length and propagates towards its lower edge. This is also observed in the DIC measurements, where a crack at the same location starts on the backside of the cylinder (region not covered by DIC cameras) and propagates towards the cylinder lower edge. No buckling evidence has been observed for the VAFW8 specimen.

The maximum compressive load (F_C), stiffness (K — calculated at a shortening level of 1 mm), and absorbed energy (E — calculated by integrating each curve) for all configurations are compiled in Table 5. Although all calculated parameters increase in the following order MA < CA < VAFW4, they do not differ statistically. Nevertheless, cylinder VAFW8 shows a significant enhancement for all three comparison parameters, which corroborates the great potential of VAFW fiber path to improve the performance of composite shells under axial compression.

Table 5
Average maximum compressive load, stiffness, and absorbed energy, and the respective standard deviations: Experimental and predicted values.

Design	F_C [kN]			K [kN/mm]			E [J]		
	Exp.	Num.	Dif.	Exp.	Num.	Dif.	Exp.	Num.	Dif.
MA	11.8 ± 1.4	11.9	0.8%	5.8 ± 0.1	5.9	1.4%	14.6 ± 3.9	13.3	9.6%
CA	12.5 ± 0.8	13.0	4.2%	5.9 ± 0.4	5.9	3.6%	14.3 ± 1.3	13.9	2.4%
VAFW4	13.5 ± 1.1	14.2	4.7%	6.4 ± 0.4	6.4	0.2%	17.9 ± 7.0	16.0	11.7%
VAFW8	20.5 ± 3.8	21.8	6.4%	8.5 ± 1.4	8.5	3.3%	25.7 ± 6.1	27.2	5.6%

Relative difference (Dif.) = (|Exp. − Num.|) ×100/Num.

In terms of absolute properties, as per Table 5, its average experimental compressive strength is 74%, 64%, and 52% higher than the MA, CA, and VAFW4 cylinders, respectively. This is a strong indication that appropriately varying the fiber orientation can enhance the distribution of stresses when approaching the bifurcation point.

Table 5 also presents the predictions from the nonlinear FE models with progressive damage and imperfections incorporated. Generally speaking, all predictions are within the standard deviation from experimental values, which demonstrates the high fidelity achieved by the developed models. In terms of maximum compressive load, the highest relative difference between numerical predictions (*Num.* in Table 5) and experimental results (*Exp.* in Table 5) are of 6.4%, whereas the difference for the MA cylinder is only 0.8%. As expected, the stiffness predictions are even closer to the experimental measurements, in which the highest difference is of 3.3% for the VAFW8 design, and as low as 0.2% for the VAFW4 cylinder. A similar panorama is seen for the

Table 6
Average experimental and predicted specific properties.

Design	F_C^S [kN/g]				K^S [kN/mm g]				E^S [J/g]			
	Exp.	Imp.	Num.	Imp.	Exp.	Imp.	Num.	Imp.	Exp.	Imp.	Num.	Imp.
MA	0.080	–	0.080	–	0.039	–	0.040	–	0.099	–	0.090	–
CA	0.086	7.4%	0.089	11.2%	0.040	3.1%	0.042	5.5%	0.098	−1.3%	0.085	5.7%
VAFW4	0.091	13.6%	0.095	18.3%	0.043	9.6%	0.043	8.3%	0.120	21.2%	0.107	19.0%
VAFW8	0.124	55.8%	0.132	64.4%	0.052	31.5%	0.053	34.1%	0.156	57.4%	0.165	82.7%

Imp.: = Improvement in relation to cylinder MA.
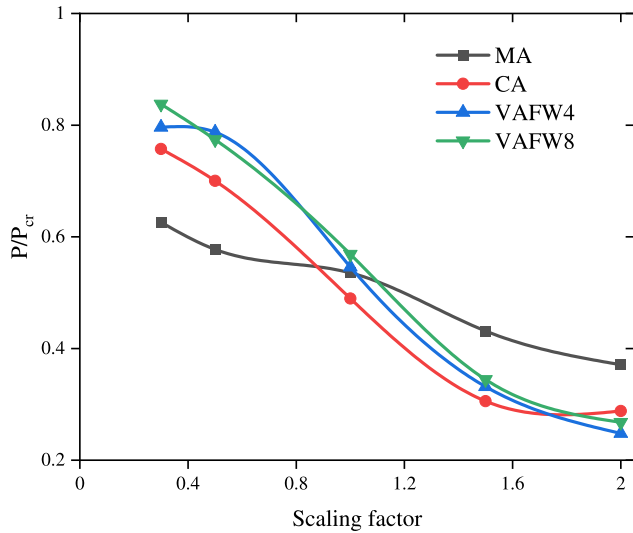
Fig. 17. Imperfection sensitivity (knockdown) curves for all cylinders.

absorbed energy, where the largest difference of 11.7% is observed for the VAFW4 cylinder.

In order to compare the calculated mechanical properties for the different cylinders using a better basis, the properties are normalized using the mass of each cylinder, given in Table 3. The calculated specific properties are presented in Table 6. For maximum specific compressive force (F_C^S), specific stiffness (K^S), and specific absorbed energy (E^S), the highest improvements are always for the cylinder VAFW8. This confirms that the amount of material placed in this design is not decisive in its properties, but instead the variable-angle fiber configuration that provides an effective fiber distribution that enhance the compressive strength of the VAFW8 shell.

A numerical study to quantify the imperfection sensitivity of the cylinders is conducted by applying a scaling factor (SF) to the measured imperfections of Fig. 8. The scaling factor is varied from 0.3 to 2.0, affecting both the mid-surface and thickness imperfections. The scaled imperfections are applied to the models described in Section 4, and the analyses are performed as before. Fig. 17 presents knockdown curves generated with the knockdown factor defined as P/P_{cr} [46]; where P is the failure load obtained from the nonlinear simulation; and P_{cr} the first linear buckling eigenvalue, given in Table 2 for each design. The curves reveal that design MA is the least sensitive, seen by the gradient of P/P_{cr} with respect to SF at the region around $SF = 1$. The other three designs show comparable sensitivity, and it is observed that the previously reported failure modes remain the same, starting with a local imperfection-driven instability that immediately leads to strain levels beyond the material allowable, yielding permanent damage. Larger imperfection amplitudes result in the appearance of instabilities at lower load levels, thus justifying the lower P values.

6. Conclusions

In this work, variable-angle cylinders were manufactured for the first time through filament winding process. The designs consist of

varying the fiber angle along the axial direction of the shell. The cylinders were optimized using a genetic algorithm. Axial compression tests assisted by DIC have been carried out to capture displacement and strain fields of the specimens. In addition, the thickness geometric imperfection patterns have also been measured via DIC. These imperfections are then incorporated into nonlinear FE models whereby a progressive damage model is employed to predict the load-shortening response and failure mechanism of the cylinders. An imperfection sensitivity analysis has also been performed.

The cylinder VAFW8 showed an average compressive strength 74% higher than the baseline constant-angle shells, being also stiffer and able to absorb more energy during the compression tests. The optimum fiber path configuration of this design revealed a thickness buildup along the helical cross-over zones, which along with the optimum arrangement of winding angles in particular regions yielded the best design. Results from thickness measurements supported the fact that the helical cross-over zones act as regions of strain concentrations and ultimately as imperfections imprinted onto the cylinder. Analysis of the damage pattern from simulations, and the displacement and strain fields from DIC, indicated that MA and VAFW4 cylinders failed predominantly by buckling, whereas cylinders CA and VAFW8 buckled and subsequently reached material failure mainly due to matrix compression and matrix tension damage mechanisms. Also, fiber compression damage index is triggered for cylinder CA, whilst both fiber tension and compression damage indices also degrade throughout the simulation. Furthermore, the numerical imperfection sensitivity analysis showed that the CA, VAFW4 and VAFW8 cylinders have the highest imperfection sensitivity, whereas the non-optimized MA shell has the lowest.

To exploit the full potential of VAFW cylinders one must be able to tailor the stiffness and buckling performance using a suitable design parameterization and optimizing the winding angles and tow overlapping pattern to postpone buckling and better exploit material strength, as demonstrated here. Future studies should quantify the effect of the scatter in manufacturing parameters and material properties on the performances of VAFW cylinders, while also investigating reliability-based design and optimization considering this scatter. Finally, the potential of VAFW designs to enable imperfection insensitive structures for space applications is still unknown and the design parameterization concepts herein presented open a wide range of possibilities for achieving less conservative designs.

CRediT authorship contribution statement

José Humberto S. Almeida Jr.: Conceptualization, Methodology, Software, Validation, Formal analysis, Investigation, Data curation, Visualization, Writing - original draft, Writing - review & editing. **Luc St-Pierre:** Writing - review & editing, Supervision. **Zhihua Wang:** Investigation. **Marcelo L. Ribeiro:** Software, Formal analysis. **Volnei Tita:** Writing - review & editing. **Sandro C. Amico:** Resources, Writing - review & editing, Funding acquisition. **Saullo G.P. Castro:** Conceptualization, Methodology, Resources, Supervision, Software, Validation, Investigation, Data curation, Visualization, Writing - original draft, Writing - review & editing.

Declaration of competing interest

The authors declare that they have no known competing financial interests or personal relationships that could have appeared to influence the work reported in this paper.

Acknowledgments

References

[1] Huang Z, Qian X, Su Z, Pham DC, Sridhar N. Experimental investigation and damage simulation of large-scaled filament wound composite pipes. Composites B 2020;184:107639. http://dx.doi.org/10.1016/j.compositesb.2019.107639.

[2] Almeida Jr JHS, Faria H, Marques A, Amico S. Load sharing ability of the liner in type III composite pressure vessels under internal pressure. J Reinf Plast Compos 2014;33(24). http://dx.doi.org/10.1177/0731684414560221.

[3] Perillo G, Grytten F, Sørbø S, Delhaye V. Numerical/experimental impact events on filament wound composite pressure vessel. Composites B 2015;69:406–17. http://dx.doi.org/10.1016/j.compositesb.2014.10.030.

[4] Cui Z, Liu Q, Sun Y, Li Q. On crushing responses of filament winding CFRP/aluminum and GFRP/CFRP/aluminum hybrid structures. Composites B 2020;200:108341. http://dx.doi.org/10.1016/j.compositesb.2020.108341.

[5] Almeida Jr JHS, Tonatto ML, Ribeiro ML, Tita V, Amico SC. Buckling and post-buckling of filament wound composite tubes under axial compression: Linear, nonlinear, damage and experimental analyses. Composites B 2018;149:227–39. http://dx.doi.org/10.1016/j.compositesb.2018.05.004.

[6] Gemi L, Köklü U, Yazman Ş, Morkavuk S. The effects of stacking sequence on drilling machinability of filament wound hybrid composite pipes: Part-1 mechanical characterization and drilling tests. Composites B 2020;186:107787. http://dx.doi.org/10.1016/j.compositesb.2020.107787.

[7] Stedile Filho P, Almeida Jr JHS, Amico SC. Carbon/epoxy filament wound composite drive shafts under torsion and compression. J Compos Mater 2018;52(8):1103–11. http://dx.doi.org/10.1177/0021998317722043.

[8] Wang Q, Li T, Wang B, Liu C, Huang Q, Ren M. Prediction of void growth and fiber volume fraction based on filament winding process mechanics. Compos Struct 2020;246:112432. http://dx.doi.org/10.1016/j.compstruct.2020.112432.

[9] Rafiee R. On the mechanical performance of glass-fibre-reinforced thermosetting-resin pipes: A review. Compos Struct 2016;143:151–64. http://dx.doi.org/10.1016/j.compstruct.2016.02.037.

[10] Wang Z, Almeida Jr JHS, St-Pierre L, Wang Z, Castro SGP. Reliability-based buckling optimization with an accelerated kriging metamodel for filament-wound variable angle tow composite cylinders. Compos Struct 2020;254:112821. http://dx.doi.org/10.1016/j.compstruct.2020.112821.

[11] Wang Z, Almeida, Jr. JHS, Ashok A, Wang Z, Castro SGP. Lightweight design of variable-angle filament-wound cylinders combining kriging-based metamodels with particle swarm optimization. 2021, http://dx.doi.org/10.31224/osf.io/3ym95, Preprint.

[12] Almeida Jr JHS, Bittrich L, Spickenheuer A. Improving the open-hole tension characteristics with variable-axial composite laminates: Optimization, progressive damage modeling and experimental observations. Compos Sci Technol 2020;185:107889. http://dx.doi.org/10.1016/j.compscitech.2019.107889.

[13] Kim BC, Potter K, Weaver PM. Continuous tow shearing for manufacturing variable angle tow composites. Composites A 2012;43(8):1347–56. http://dx.doi.org/10.1016/j.compositesa.2012.02.024.

[14] Chauncey Wu K, Turpin JD, Gardner NW, Stanford BK, Martin RA. Structural characterization of advanced composite tow-steered shells with large cutouts. In: 56th AIAA/ASCE/AHS/ASC structures, structural dynamics, and materials conference. American Institute of Aeronautics and Astronautics Inc.; 2015, http://dx.doi.org/10.2514/6.2015-0966.

[15] Gürdal Z, Olmedo R. In-plane response of laminates with spatially varying fiber orientations: Variable stiffness concept. AIAA J 1993;31(4):751–8. http://dx.doi.org/10.2514/3.11613.

[16] Guimarães TAM, Castro SGP, Cesnik CES, Rade DA. Supersonic flutter and buckling optimization of tow-steered composite plates. AIAA J 2018;57(1):397–407. http://dx.doi.org/10.2514/1.J057282.

[17] Castro SGP, Donadon MV, Guimarães TA. ES-PIM applied to buckling of variable angle tow laminates. Compos Struct 2019;209:67–78. http://dx.doi.org/10.1016/j.compstruct.2018.10.058.

[18] Hao P, Liu C, Yuan X, Wang B, Li G, Zhu T, et al. Buckling optimization of variable-stiffness composite panels based on flow field function. Compos Struct 2017;181:240–55. http://dx.doi.org/10.1016/j.compstruct.2017.08.081.

[19] Hao P, Yuan X, Liu C, Wang B, Liu H, Li G, et al. An integrated framework of exact modeling, isogeometric analysis and optimization for variable-stiffness composite panels. Comput Methods Appl Mech Engrg 2018;339:205–38. http://dx.doi.org/10.1016/j.cma.2018.04.046.

[20] Hao P, Wang Y, Ma R, Liu H, Wang B, Li G. A new reliability-based design optimization framework using isogeometric analysis. Comput Methods Appl Mech Engrg 2019;345:476–501. http://dx.doi.org/10.1016/j.cma.2018.11.008.

[21] Hao P, Liu D, Wang Y, Liu X, Wang B, Li G, et al. Design of manufacturable fiber path for variable-stiffness panels based on lamination parameters. Compos Struct 2019;219:158–69. http://dx.doi.org/10.1016/j.compstruct.2019.03.075.

[22] Tatting BF. Analysis and Design of Variable Stiffness Composite Cylinders in Engineering Mechanics. Tech. rep., Virginia Tech; 1998, http://hdl.handle.net/10919/29313.

[23] Blom AW, Stickler PB, Gürdal Z. Design and manufacture of a variable-stiffness cylindrical shel. Tech. rep., SAMPE Europe; 2009, p. 1–8, URL https://repository.tudelft.nl/islandora/object/uuid%3A0d8a5de7-966a-4f80-bc5c-bc66b1733410.

[24] Blom AW, Rassaian M, Stickler PB, Gürdal Z. Modal testing of a composite cylinder with circumferentially varying stiffness. In: Collection of technical papers - AIAA/ASME/ASCE/AHS/ASC structures, structural dynamics and materials conference. American Institute of Aeronautics and Astronautics Inc.; 2009, p. 1–15. http://dx.doi.org/10.2514/6.2009-2558.

[25] Blom AW, Stickler PB, Gürdal Z. Optimization of a composite cylinder under bending by tailoring stiffness properties in circumferential direction. Composites B 2010;41(2):157–65. http://dx.doi.org/10.1016/j.compositesb.2009.10.004.

[26] Blom AW. Structural performance of fiber-placed, variable-stiffness composite conical and cylindrical shells (Ph.D. thesis), TU Delft; 2010, p. 1–260, http://resolver.tudelft.nl/uuid:46f2e44b-1a68-44f8-9633-79490a54e087.

[27] Wu KC, Tatting BF, Smith BH, Stevens RS, Occhipinti GP, Swift JB, et al. Design and manufacturing of tow-steered composite shells using fiber placement. In: Collection of technical papers - AIAA/ASME/ASCE/AHS/ASC structures, structural dynamics and materials conference. American Institute of Aeronautics and Astronautics Inc.; 2009, http://dx.doi.org/10.2514/6.2009-2700.

[28] Wu KC, Stanford BK, Hrinda GA, Wang Z, Martin RA, Alicia Kim H. Structural assessment of advanced composite tow-steered shells. In: 54th AIAA/ASME/ASCE/AHS/ASC structures, structural dynamics, and materials conference. 2013, http://dx.doi.org/10.2514/6.2013-1769.

[29] White SC, Weaver PM, Wu KC. Post-buckling analyses of variable-stiffness composite cylinders in axial compression. Compos Struct 2015;123:190–203. http://dx.doi.org/10.1016/j.compstruct.2014.12.013.

[30] Wu KC, Farrokh B, Stanford B, Weaver P. Imperfection insensitivity analyses of advanced composite tow-steered shells. In: 57th AIAA/ASCE/AHS/ASC structures, structural dynamics, and materials conference. Reston, Virginia: American Institute of Aeronautics and Astronautics; 2016, http://dx.doi.org/10.2514/6.2016-1498.

[31] Rouhi M, Ghayoor H, Fortin-Simpson J, Zacchia TT, Hoa SV, Hojjati M. Design, manufacturing, and testing of a variable stiffness composite cylinder. Compos Struct 2018;184:146–52. http://dx.doi.org/10.1016/j.compstruct.2017.09.090.

[32] Castro SGP, Almeida Jr JHS, St-Pierre L, Wang Z. Measuring geometric imperfections of variable–angle filament–wound cylinders with a simple digital image correlation (DIC) set up. Compos Struct 2021;114497. http://dx.doi.org/10.1016/j.compstruct.2021.114497.

[33] Vertonghen L, Castro SG. Modelling of fibre steered plates with coupled thickness variation from overlapping continuous tows. Compos Struct 2021;113933. http://dx.doi.org/10.1016/j.compstruct.2021.113933.

[34] Almeida Jr JHS, Souza SD, Botelho EC, Amico SC. Carbon fiber-reinforced epoxy filament-wound composite laminates exposed to hygrothermal conditioning. J Mater Sci 2016;51(9):4697–708. http://dx.doi.org/10.1007/s10853-016-9787-9.

[35] Barbero EJ, Cosso FA, Roman R, Weadon TL. Determination of material parameters for abaqus progressive damage analysis of E-glass epoxy laminates. Composites B 2013;46:211–20. http://dx.doi.org/10.1016/j.compositesb.2012.09.069.

[36] Castro SGP, Mittelstedt C, Monteiro FA, Arbelo MA, Ziegmann G, Degenhardt R. Linear buckling predictions of unstiffened laminated composite cylinders and cones under various loading and boundary conditions using semi-analytical models. Compos Struct 2014;118(1):303–15. http://dx.doi.org/10.1016/j.compstruct.2014.07.037.

[37] Castro SGP, Donadon MV. Assembly of semi-analytical models to address linear buckling and vibration of stiffened composite panels with debonding defect. Compos Struct 2017;160:232–47. http://dx.doi.org/10.1016/j.compstruct.2016.10.026.

[38] Almeida Jr JHS, Bittrich L, Nomura T, Spickenheuer A. Cross-section optimization of topologically-optimized variable-axial anisotropic composite structures. Compos Struct 2019;225. http://dx.doi.org/10.1016/j.compstruct.2019.111150.

[39] Kogiso N, Watson LT, Gürdal Z, Haftka RT. Genetic algorithms with local improvement for composite laminate design. Struct Optim 1994;7(4):207–18. http://dx.doi.org/10.1007/BF01743714.

[40] Dalibor IH, Lisbôa TV, Marczak RJ, Amico SC. Optimum slippage dependent, non-geodesic fiber path determination for a filament wound composite nozzle. Eur J Mech A Solids 2020;82:103994. http://dx.doi.org/10.1016/j.euromechsol.2020.103994.

[41] Zu L, Koussios S, Beukers A. Shape optimization of filament wound articulated pressure vessels based on non-geodesic trajectories. Compos Struct 2010;92(2):339–46. http://dx.doi.org/10.1016/j.compstruct.2009.08.013.

[42] Lisbôa TV, Almeida Jr JHS, Dalibor IH, Spickenheuer A, Marczak RJ, et al. The role of winding pattern on filament wound composite cylinders under radial compression. Polym Compos 2020;41(6):2446–54. http://dx.doi.org/10.1002/pc.25548.

[43] Castro SGP, Almeida Jr JHS. VAFW cylinders 2020, S1, S2, S4, S8, DIC raw data, Version 2021-03-16; 2021. http://dx.doi.org/10.5281/zenodo.4608398.

[44] Castro SGP, Almeida Jr JHS. VAFW cylinders 2020, S1, S2, S4, S8, stitched imperfections, Version 2021-03-04; 2021. http://dx.doi.org/10.5281/zenodo.4581164.

[45] Croll JG. Towards a rationally based elastic-plastic shell buckling design methodology. Thin-Walled Struct 1995;23(1–4):67–84. http://dx.doi.org/10.1016/0263-8231(95)00005-X.

[46] Castro SG, Zimmermann R, Arbelo MA, Khakimova R, Hilburger MW, Degenhardt R. Geometric imperfections and lower-bound methods used to calculate knock-down factors for axially compressed composite cylindrical shells. Thin-Walled Struct 2014;74:118–32. http://dx.doi.org/10.1016/j.tws.2013.08.011.

[47] Castro SGP, Reichardt J, Lozano E. DESICOS plug-in for abaqus. Version 2.4.13. 2021, http://dx.doi.org/10.5281/zenodo.4506587.

[48] Hashin Z. Fatigue failure criteria for unidirectional fiber composites. J Appl Mech Trans ASME 1981;48(4):846–52. http://dx.doi.org/10.1115/1.3157744.

[49] Matzenmiller A, Lubliner J, Taylor RL. A constitutive model for anisotropic damage in fiber-composites. Mech Mater 1995;20(2):125–52. http://dx.doi.org/10.1016/0167-6636(94)00053-0.